RSC Advances

PAPER

View Article Online
View Journal | View Issue

Cite this: *RSC Adv.*, 2021, **11**, 31631

Structural, optical and dielectric properties of tellurium-based double perovskite $Sr_2Ni_{1-x}Zn_xTeO_6$

Fatasya Izreen Hanim Alias,[a] Rozilah Rajmi,[b] Mohd Fauzi Maulud[a] and Zakiah Mohamed *[a]

In this paper, $Sr_2Ni_{1-x}Zn_xTeO_6$ (x = 0.0, 0.2, 0.4, 0.6, 0.8, 1.0) double perovskite compounds were synthesised by the conventional solid-state method, and the structural, optical and dielectric properties were investigated. The Rietveld refinement of X-ray diffraction data shows that all compounds were crystallised in monoclinic symmetry with the *I*2/*m* space group. Morphological scanning electron microscopy reported that the grain sizes decreased as the dopant increased. The UV-vis diffuse reflectance spectroscopy conducted for all samples found that the optical band gap energy, E_g, increased from 3.71 eV to 4.14 eV. The dielectric permittivity ε' values increased for the highest Zn-doped composition, $Sr_2Ni_{0.2}Zn_{0.8}TeO_6$, being ~1000 and ~60 in the low- and high-frequency range, respectively. All samples exhibited low dielectric loss ($\tan\delta \leq 0.20$) in the range of 10^4–10^5 Hz frequency. Impedance measurement revealed that grain resistance decreased with enhancement in Zn content in the Sr_2NiTeO_6 crystal lattice.

Received 10th May 2021
Accepted 18th September 2021

DOI: 10.1039/d1ra03662a

rsc.li/rsc-advances

Introduction

Double perovskite oxides with the formula $AA'BB'O_6$ (A = alkaline, alkaline-earth or rare-earth ions; B and B′ = transition metal ions) are derived from simple perovskite oxides, ABO_3, and they have been extensively investigated due to their fascinating physical properties and potential applications in superconductivity, ferroelectricity, dielectricity and magnetoelectricity. Several of them exhibit half-metallic ferromagnetism with a high spin polarisation at the Fermi level that is appropriate for future spin electronics.[1]

Recently, tellurium (Te)-based double perovskite oxides have attracted the attention of researchers due to their structural features and technological applications in various fields, such as microwave communication devices. As reported by previous study, the Te^{6+} ion is one of p-block elements that can be strongly stabilized in B-site of perovskite structure while preserving required spherical symmetry and adequate ion size.[2] Other than that, Te-based double perovskites showed excellent microwave properties with very low sintering temperatures (>700 °C).[3] The Sr_2ZnTeO_6 double perovskite presented intrinsic quality factor × frequency and dielectric constant of 85 THz and 14.1, respectively.[4] Dias *et al.* reported that the microwave dielectric values of different A-site doped Te-based double perovskites, Ba_2MgTeO_6, Sr_2MgTeO_6 and Ca_2MgTeO_6, were 11.61, 14.31 and 13.23, respectively.[3] Mixed doping of Te-double perovskite oxides, $Sr_{2-x}Ca_xMgTeO_6$, reported by Ubic *et al.* showed microwave dielectric permittivities in the range of 13.2–14.3.[5] These microwave dielectric results could be associated with the tolerance factor, volume, density and polarisability aspects.[6] Therefore, Te-based double perovskites are promising candidates for microwave applications.

Moreover, B-site doped double perovskite has the potential to be excellent in dielectric or ferroelectric devices. Zhao *et al.* stated that the microwave dielectric constants of A_2BWO_6 (A = Sr, Ba; B = Co, Ni, Zn) double perovskites were between 18.1–29.1. These values showed that the dielectric constant increased when increasing B^{2+} ionic polarisability was enhanced due to the increase in B-site ordering.[7] In addition, Vilesh *et al.* reported that the dielectric properties of Te-based double perovskites, $BaBiNaTeO_6$ and $BaLaNaTeO_6$, possessed high dielectric values, which were 39.7 and 18.5, respectively at 1 MHz.[8] The high dielectric values were related to the high density and large grain size. Dielectric measurement was performed on Sr_2NiTeO_6 and Sr_2NiWO_6 double perovskite compound, and showed a high value of dielectric constant (341 and 308, respectively) with low dielectric loss (0.06 and 0.23, respectively) at 1 kHz frequency.[6]

Particularly, the properties of $A_2BB'O_6$ are affected by the cation ordering, the octahedral distortion and the distribution of the B and B′ cations over the octahedral sites. Other variables that control the properties of $A_2BB'O_6$ include the degree of cation inversion and the size and electronic structure of

[a]*Faculty of Applied Sciences, Universiti Teknologi MARA, 40450, Shah Alam, Selangor, Malaysia. E-mail: zakiah626@uitm.edu.my*

[b]*Faculty of Applied Sciences, Universiti Teknologi MARA, Perlis Branch, Arau Campus, 02600 Arau, Perlis, Malaysia*

transition metal B and B′ cations. Thus, the B and B′ ions determine the physical properties of compounds, including the magnetic and optical properties. The magnetic and optical properties of double perovskite with Te-based, $SrLa_{1-x}Nd_x$-$LiTeO_6$ were reported to be in paramagnetic behaviour at room temperature, and the energy bandgap decreased as the doping increased.[6,9] Moreover, various kinds of B and B′ cation pairs show different of physical properties of perovskites. Tokura *et al.* reported that Sr_2FeMoO_6 and Sr_2MnMoO_6 were ferromagnetic and antiferromagnetic, respectively.[10,11]

In the previous study, the effect of Sr^{2+} ion substitution on the Ba site of Ba_2ZnWO_6 double perovskite in optical properties was determined, and the results showed that the energy band gap decreased from 3.27 eV to 3.07 eV. From this range of energy band gap values, the compounds were classified as high-band-gap semiconductor materials suitable for solar cell applications.[12]

Although several new Te-based double perovskite materials were reported, to the best of our knowledge, no investigation has been conducted to explore the structural, optical and dielectric properties of complex double perovskites with Ni, Zn and Te in their composition. In this work, the results of X-ray diffraction (XRD), scanning electron microscopy (SEM), Fourier transform infrared (FTIR) spectroscopy, UV-vis diffuse reflectance and dielectric study of $Sr_2Ni_{1-x}Zn_xTeO_6$ ($x = 0.0$, 0.2, 0.4, 0.6, 0.8, 1.0) double perovskite compounds are reported and discussed.

Experimental

Polycrystalline powders of $Sr_2Ni_{1-x}Zn_xTeO_6$ ($x = 0.0$, 0.2, 0.4, 0.6, 0.8, 1.0) were synthesised using the conventional solid-state reaction technique. Stoichiometric amounts of strontium carbonate, $SrCO_3$ (99.9%), nickel oxide, NiO (99.9%), zinc oxide, ZnO (99.9%) and tellurium dioxide, TeO_2 (99.9%) were mixed and ground for an hour in an agate mortar with a pestle to achieve good homogeneity. The mixed powders were then placed on an alumina crucible and calcinated in a box furnace at 900 °C for 12 h at a heating rate of 15 °C min^{-1} and a cooling rate of 1°C min^{-1}. Afterwards, the samples were ground again for an hour, formed into pellets of disk shape and sintered at 1150 °C for 24 h in air atmosphere.

The phase of the final products was analysed using the XRD patterns collected by an X-ray powder diffractometer (PANalytical model Xpert PRO MPD diffractometer) equipped with a Cu-K_α source ($\lambda = 1.5406$ Å) at room temperature with a scattering angle range of 20–80°. The data were collected with a step size of 0.017° and a counting time of 18 s per step. General Structure Analysis System and a Graphical User Interface (*i.e.* EXPGUI)[13,14] programmes were used for Rietveld refinement prior to the visualisation in the Visualisation for Electronic Structural Analysis programme. The peak shape was modelled by the pseudo Voight function refined with cell parameter, scale factor, zero factor and background function.

The surface morphology and homogeneity of the perovskite samples were obtained using SEM equipment, LEO model 982 Gemini measurement with energy-dispersive spectroscopy (EDX). The magnification of SEM micrograph used was ×5k, and the grain size was measured by ImageJ software. The FTIR analysis ranging from 450 cm^{-1} to 1000 cm^{-1} was recorded with FTIR-Raman Drift Nicolet 6700 equipment. A UV-vis spectrophotometer (Cary 500 UV-vis-NIR) using PbSmart as detector and controlled by the Cary WinUV software was used to calculate the UV-vis diffuse reflectance spectrum at room temperature. In addition, the UV-vis reflectance spectrum was converted into absorbance using the Kubelka–Munk method to estimate the edge of absorption and band gap of the Sr_2Ni_{1-x} Zn_xTeO_6 double perovskite series. The impedance and dielectric properties in range of 1 Hz to 10 MHz were collected using a Solartron 1286 electrochemical interface with a 1255 frequency response analyser at room temperature.

Results and discussion

XRD analysis

Fig. 1 shows the XRD profiles for $Sr_2Ni_{1-x}Zn_xTeO_6$ ($x = 0.0$, 0.2, 0.4, 0.6, 0.8, 1.0) compounds at room temperature. No extra reflection peaks were observed in the compound with $x = 1.0$, which confirms no formation of secondary phases or impurities, similar reported by Alias *et al.*[15] Samples with $x = 0.0$, 0.2, 0.4, 0.6, 0.8 have small impurity peaks that consist of excess Sr_3TeO_6. The XRD data of each samples were refined by the Rietveld refinement method, as depicted in Fig. 2. The Rietveld refinement revealed that all the compounds are in monoclinic unit cell in the *I*2/*m* space group, as reported by previous study.[16,17] The refined lattice angles for all compounds are $\alpha = \gamma = 90°$, whereas β for $x = 0.0$, 0.2, 0.4, 0.6, 0.8, 1.0 are 90.018, 90.063, 90.046, 90.111, 90.141 and 90.063°, respectively; the refined unit cell volumes (V) of each samples are 247.580, 248.241, 248.692, 250.580, 251.199 and 252.042 $Å^3$, respectively. These results show that the unit cell volume of the crystal structure increases as the doping increases from $x = 0.0$ to $x = 1.0$. In general, the increase in unit cell volume is associated with the ionic radius. Therefore, the result is consistent for

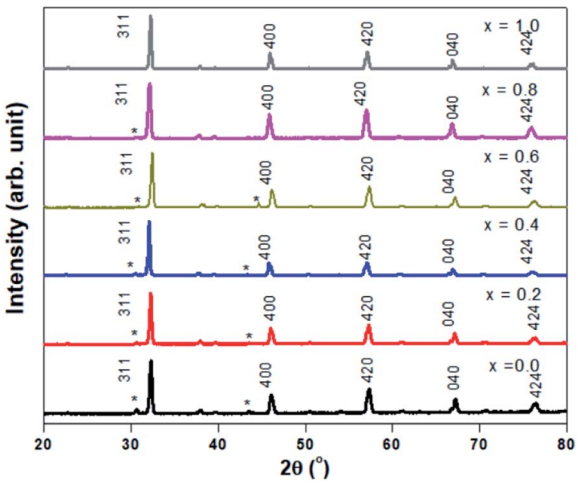

Fig. 1 XRD pattern of $Sr_2Ni_{1-x}Zn_xTeO_6$ ($x = 0.0$, 0.2, 0.4, 0.6, 0.8, 1.0) with (*) labelled as Sr_3TeO_6.

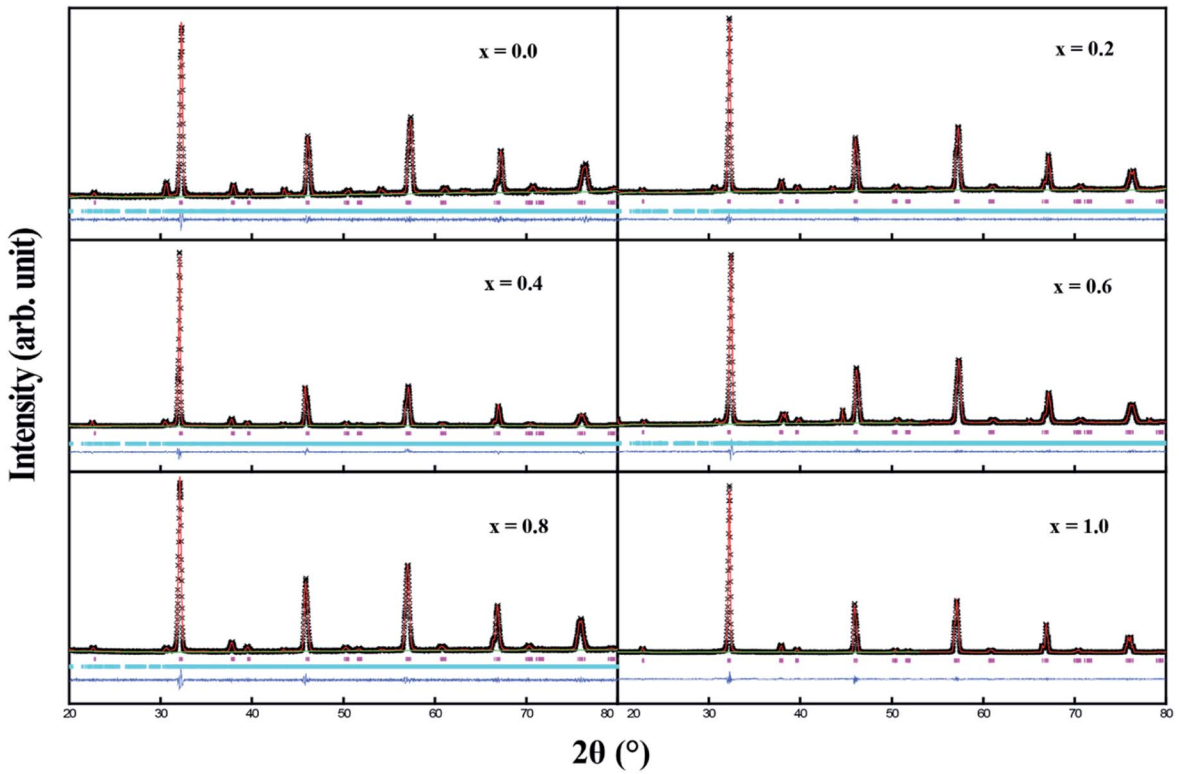

Fig. 2 Rietveld refinement of XRD pattern for $Sr_2Ni_{1-x}Zn_xTeO_6$ (x = 0.0, 0.2, 0.4, 0.6, 0.8, 1.0). Black scattered symbols are observed data, the solid red line is the calculated pattern and the blue solid line is the difference. Pink and blue tick marks indicate the allowed Bragg reflections for primary and secondary phases, respectively.

codoped compound whose ionic radius of Zn^{2+} is greater than Ni^{2+}, with 0.74 Å and 0.69 Å, respectively.

The lattice parameters for all compounds are presented in Table 1. Fig. 3 illustrates the octahedral structure that consists of Ni^{2+} and Te^{6+} as B and B′ cations, respectively, surrounded alternately by six O^{2-} atoms whilst Sr^{2+} as A cations fill the occupancy between these $NiTeO_6$ octahedral layers. Tolerance factor τ is used to predict the stability of the perovskite structure and given as eqn (1):

$$\tau = \frac{r_A + r_O}{\sqrt{2}\left(\left(\frac{r_B + r_{B'}}{2}\right) + r_O\right)} \quad (1)$$

where r_A is the ionic radii of the A cation, which is Sr^{2+} (1.44 Å); r_B and $r_{B'}$ are the ionic radii of B and B′ cations, which are Ni^{2+}/Zn^{2+} (0.69 Å/0.74 Å) and Te^{6+} (0.56 Å), respectively; and r_O is ionic radii of O^{2-} (1.40 Å). The τ of the ideal crystal structure is 1. The value of τ or $Sr_2Ni_{1-x}Zn_xTeO_6$, x = 0.0, 0.2, 0.4, 0.6, 0.8, 1.0 are 0.9844, 0.9893, 0.9869, 0.9844, 0.9820 and 0.9796, respectively, indicating ion distortion within all compounds as large size of Zn^{2+} cation is doped in the compound. The average bond length of Ni/Zn–O for all compounds slightly changes with Zn concentration. Different average bond lengths in each compound cause the bond angles between octahedral B sites Ni/Zn–O–Te to increase from 158.6655° to 166.7800° for x = 0.0 to x = 1.0 due to a small change of octahedral structure distortion, which is related to τ values without a structure change.

The Scherrer equation shown in eqn (2) is used to calculate the crystalline size (D):

$$D = \frac{K\lambda}{\beta(\theta)\cos\theta} \quad (2)$$

where K is a constant with 0.94; λ is the wavelength of XRD, which is 0.1541 nm for Cu-K_α radiation; $\beta(\theta)$ is the full width at half maximum in radians; and θ is the angle of the most intense peak in XRD. The D values for $Sr_2Ni_{1-x}Zn_xTeO_6$, x = 0.0, 0.2, 0.4, 0.6, 0.8, 1.0 are 30.6307, 29.7252, 30.6268, 34.7859, 22.5119 and 36.0399 nm, respectively, as listed in Table 1. The increase in crystalline size from 29.7252 nm for x = 0.2 to 34.7859 nm for x = 0.6 represents that Zn^{2+} dopant provides the better crystallisation as doping concentrations increase. The crystalline size of the compound is comparable with other Te-based double perovskites, $SrLaLiTeMnO_6$ and $SrLaLiNdTeO_6$, in range of 20–29 and 28–42 nm, respectively.[6,18]

Morphology

The SEM images of the $Sr_2Ni_{1-x}Zn_xTeO_6$ (x = 0.0, 0.2, 0.4, 0.6, 0.8, 1.0) series are illustrated in Fig. 4. The morphologies of the samples obtained from the SEM images reveal that the surface of the samples are almost identical and moderately homogenous. Moreover, in all samples, the size of the particles is large, and they are aggregated in groups due to the higher preparation temperature; the same effect of temperature was observed in the morphology analysis by Lan *et al.* and Alsabah *et al.* with series

Table 1 Lattice parameters, unit cell volume, bond angles, bond lengths, fit goodness and tolerance factor (τ) in $Sr_2Ni_{1-x}Zn_xTeO_6$ (x = 0.0, 0.2, 0.4, 0.6, 0.8 and 1.0) as obtained from Rietveld refinement and crystallite size from XRD characterisation

Compounds	$x = 0.0$	$x = 0.2$	$x = 0.4$	$x = 0.6$	$x = 0.8$	$x = 1.0$
Lattice parameters						
a (Å)	5.6219(13)	5.6272(9)	5.6309(8)	5.6078(10)	5.6474(12)	5.6527(6)
b (Å)	5.5852(15)	5.5903(10)	5.5935(9)	5.6451(8)	5.6137(13)	5.6196(8)
c (Å)	7.8849(18)	7.8912(12)	7.8959(11)	7.9157(11)	7.9236(15)	7.9343(8)
α	90.000	90.000	90.000	90.000	90.000	90.000
β	90.018	90.063	90.046	90.111	90.141	90.063
γ	90.000	90.000	90.000	90.000	90.000	90.000
Unit cell volume (Å^3)						
Unit cell volume, V	247.580	248.241	248.692	250.580	251.199	252.042
Bond length (Å)						
2× Ni/Zn–O_1	2.1046(8)	2.0523(4)	2.0536(4)	2.0582(3)	2.0604(4)	2.0636(2)
4× Ni/Zn–O_2	2.0472(6)	2.0648(3)	2.0661(3)	2.0710(2)	2.0726(3)	2.0749(2)
<Ni/Zn–O>	2.0759(7)	2.0585(4)	2.0598(4)	2.0646(3)	2.0665(4)	2.0692(2)
Bond angle (°)						
Ni/Zn–O_1–Te	161.5140(1)	164.5530(0)	164.5520(0)	164.6530(0)	164.5610(0)	164.5670(0)
Ni/Zn–O_2–Te	155.8170(2)	168.9990(0)	168.9990(0)	169.0000(0)	168.9980(0)	168.9930(0)
<Ni/Zn–O–Te>	158.6655(2)	166.7760(0)	166.7760(0)	166.8265	166.7795(0)	166.7800(0)
Fit goodness						
χ^2	1.119	1.149	1.945	1.353	1.318	2.402
R_P (%)	0.0310	0.0280	0.0325	0.0268	0.0351	0.0389
R_{WP} (%)	0.0392	0.0361	0.0423	0.0366	0.0446	0.0513
τ	0.9844	0.9893	0.9869	0.9844	0.9820	0.9796
Crystalline size (nm)						
Crystalline size (D)	30.6307	29.7252	30.6268	34.7859	22.5119	36.0399

of La_2NiMnO_6 and $BaSrZnWO_6$, respectively.[12,19] Each sample has grain of various sizes, 1.53–1.67 μm for Sr_2NiTeO_6, 2.50–2.99 μm for $Sr_2Ni_{0.8}Zn_{0.2}TeO_6$, 2.02–2.49 μm for $Sr_2Ni_{0.6}Zn_{0.4}TeO_6$, 1.88–2.03 μm for $Sr_2Ni_{0.4}Zn_{0.6}TeO_6$, 1.23–1.38 μm for $Sr_2Ni_{0.2}Zn_{0.8}TeO_6$ and 1.20–1.38 μm for Sr_2ZnTeO_6. EDX analysis was performed with all samples using the SEM images. All EDX results presented in Fig. 4 indicate the percentage elemental composition of Sr, Ni, Zn, Te and O. The atomic percentage of Ni in pristine sample (x = 0.0) is 11.19%, which decreases as the doping content increases and becomes 3.72% (x = 0.8) and none at x = 1.0. It shows that Zn has been incorporated at the Ni site in the crystal lattice. The atomic percentages of constituent elements are tabulated in the inset of Fig. 4. The values of atomic percentage for each samples are nearly equal to the ratios of the element during sample preparation.

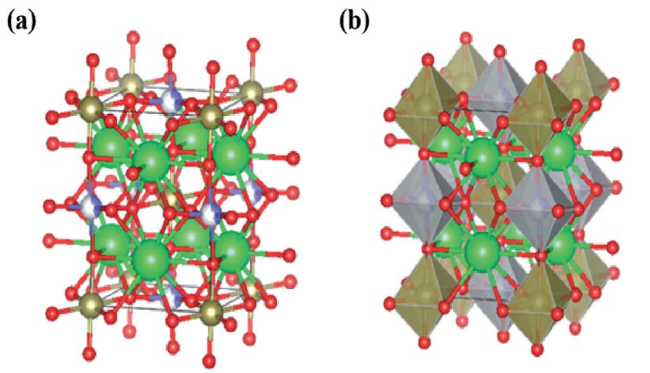

Fig. 3 (a) The crystal structure for $Sr_2Ni_{1-x}Zn_xTeO_6$ (x = 0.0, 0.2, 0.4, 0.6, 0.8 and 1.0). Sr represent as green-colored balls, Ni represent as grey-colored balls, Zn represent as blue balls and O represent as red-colored balls. (b) Structure of $SrNi_{1-x}Zn_xTeO_6$ (x = 0.0, 0.2, 0.4, 0.6, 0.8 and 1.0), where the Sr are 12-fold coordinated and Ni and Zn is 6-fold coordinated with the polyhedral.

FTIR spectroscopy

The FTIR spectra were used to identify the phase formation of the perovskite. For $Sr_2Ni_{1-x}Zn_xTeO_6$ double perovskite, the FTIR spectra of the series are similar and show a very simple spectra pattern, as usually found in perovskite materials.[20–22] The spectra revealed two distinctive absorption bands between 700–450 cm^{-1} region, as depicted in Fig. 5. The high-energy, strong band observed at around 660 cm^{-1} corresponded to the antisymmetric stretching mode of Ni–O_6, Zn–O_6 and Te–O_6 octahedral due to the higher charge of the Ni^{2+}, Zn^{2+} and Te^{4+} cations.[23] The bands that appeared around 550 cm^{-1} are suggested due to deformational modes of Ni–O_6, Zn–O_6 and Te–O_6 octahedrals. Fig. 5 shows the transmittance of the $Sr_2Ni_{1-x}Zn_xTeO_6$ double-perovskite series *versus* wave number, and all

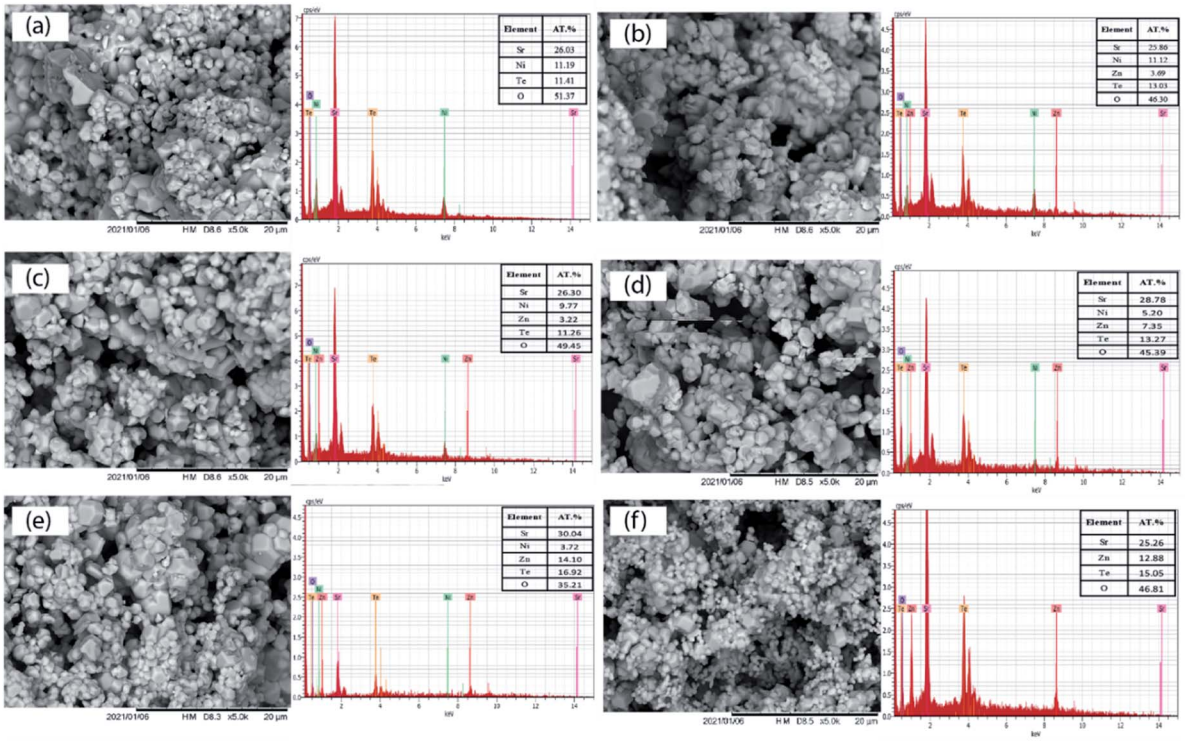

Fig. 4 Microstructures and EDX patterns of $Sr_2Ni_{1-x}Zn_xTeO_6$ (a) $x = 0.0$, (b) $x = 0.2$, (c) $x = 0.4$, (d) $x = 0.6$, (e) $x = 0.8$ and (f) $x = 1.0$.

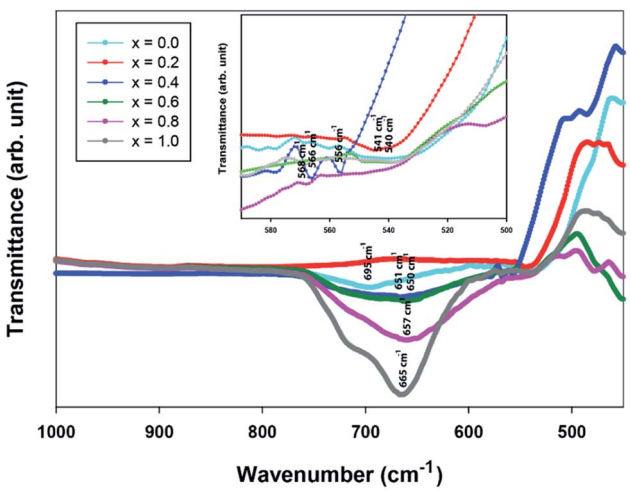

Fig. 5 FTIR spectra of $Sr_2Ni_{1-x}Zn_xTeO_6$ ($x = 0.0$, 0.2, 0.4, 0.6, 0.8 and 1.0).

the samples confirm the molecular bands on the perovskite oxide structure.

UV-visible diffuse reflectance spectroscopy

Fig. 6(a) displays the diffuse reflectance spectrum of $Sr_2Ni_{1-x}Zn_xTeO_6$ ($x = 0.0$, 0.2, 0.4, 0.6, 0.8, 1.0) in the range of 200–800 nm wavelength at 298 K. The intensity of peaks increases as the Zn content increases. A strong absorption band at 300 nm to 450 nm may be related to the charge transfer transition between doped Zn^{2+} and O^{2-} (valence and conduction band) in the lattice structure.[18,24] As Zn^{2+} increases, the increase of reflectance value of compound shows the reduction of absorbance properties. The absorption coefficient is calculated from diffuse reflectance spectra using Kubelka–Munk (KM) function, as shown in eqn (3):[12]

$$f(R) = \frac{\alpha}{s} = \frac{(1-R)^2}{2R} \quad (3)$$

where $f(R)$ represents the KM function, α is the absorption coefficient, s is the scattering coefficient and R is the reflection coefficient. The relation between absorbance $(f(R)h\nu)$ and wavelength is plotted in Fig. 6(b). By taking the intercept of the extrapolations to zero absorption with the photon energy axis, the absorption edge value can be obtained. The bandgap energy value, E_g, can be calculated by applying the following equation:

$$E_g = \frac{1240}{\lambda} \quad (4)$$

where λ represents the absorption edge wavelength. The band gap energy can be obtained directly from the x intersection of Tauc plot fitting, as illustrated in Fig. 6(c), corresponding to Tauc eqn (5):

$$[f(R)h\nu]^n = A(h\nu - E_g) \quad (5)$$

where $h\nu$ is the incident photon energy, E_g represents the band gap energy and n is the constant values of 0.5, 2, 1.5 and 3 for direct allowed, indirect allowed, direct forbidden and indirect forbidden transition, respectively.[6,24,25] This plot shows that the value of n is 0.5, and the curve has a linear part of. Therefore, the compounds

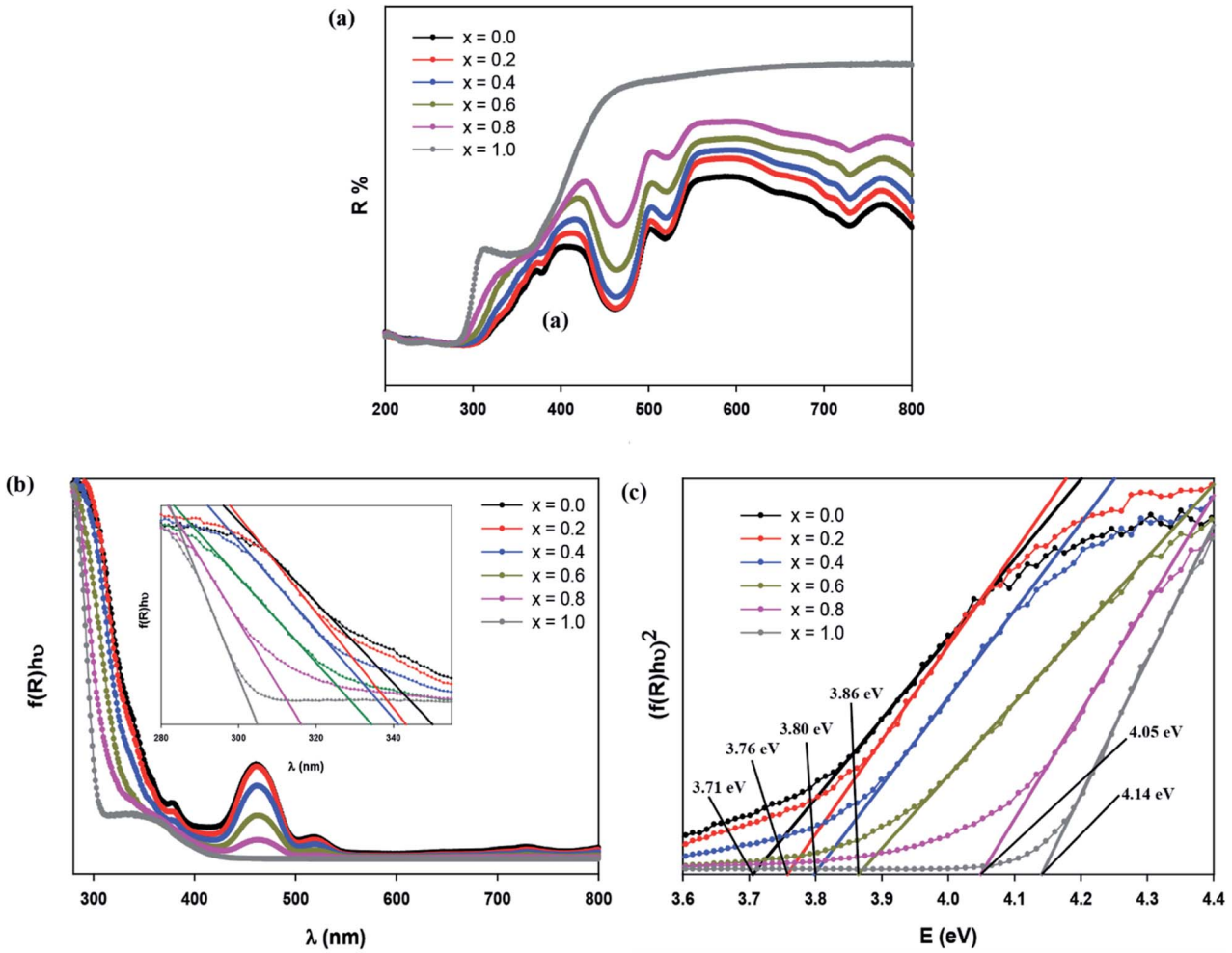

Fig. 6 (a) Diffuse reflectance spectrum, (b) Absorbance as a function of wavelength (Kubelka–Munk) plot compounds, (c) Tauc plot of $Sr_2Ni_{1-x}Zn_xTeO_6$ (x = 0.0, 0.2, 0.4, 0.6, 0.8 and 1.0) double perovskite compounds.

Table 2 Band gap energy according to the Kubelka–Munk and Tauc plot for direct transition $Sr_2Ni_{1-x}Zn_xTeO_6$ (x = 0.0, 0.2, 0.4, 0.6, 0.8 and 1.0)

Band gap energy	$x = 0.0$	$x = 0.2$	$x = 0.4$	$x = 0.6$	$x = 0.8$	$x = 1.0$
Cut-off wavelength (±0.01 nm)	350.08	343.26	341.29	334.39	316.20	304.87
E_g by cutoff wavelength (±0.01 nm)	3.54	3.61	3.63	3.71	3.92	4.07
E_g by Tauc plot (±0.01 nm)	3.71	3.76	3.80	3.86	4.05	4.14

are classified as direct band gap semiconductor, whose top of the valence band and bottom of the conduction band occur at the same value of momentum. Table 2 shows that E_g according to the KM and Tauc plot are comparable with each other. In addition, the increase in optical band gap energy value is related to the increase in Zn concentration in compound. Eng *et al.* reported that the decrease in the ionic radii of B′ site ions. In addition, the study reported that when the bond angle becomes less than 180° with octahedral tilting, an increase in bandgap is observed due to the narrowing of conduction band.[26] Zn-doped possesses high bandgap value than for Sr_2NiTeO_6 because the ionic radii for Ni^{2+} and Zn^{2+} are 2.09 and 2.14 Å, respectively.

Impedance spectroscopy analysis

To distinguish between bulk and grain boundary effect, relaxation phenomena and polarisation effect within the materials, the impedance spectroscopy (IS) method was employed from the output response of input ac signal applied across the pellet sample. The measured complex impedance (Z) has real (Z') and imaginary (Z'') components, which are interpreted as eqn (6)–(8):

$$Z^*(\omega) = (Z' - jZ'') \quad (6)$$

$$Z' = \frac{R}{1 + (\omega\tau)^2} \quad (7)$$

Table 3 Grain resistance, R_g and grain capacitance, C_g of $SrNi_{1-x}Zn_xTeO_6$ (x = 0.0, 0.2, 0.4, 0.6, 0.8 and 1.0) as obtained from Cole–Cole plot fitting with R-CPE equivalent circuit model

x	Grain resistance, R_g (10^8 Ω)	Grain capacitance, C_g (10^{-11} F)
0.0	2.097	9.380
0.2	1.925	6.638
0.4	1.099	5.768
0.6	1.002	4.972
0.8	1.012	7.853
1.0	1.336	10.879

$$Z'' = -\frac{\omega R\tau}{1+(\omega\tau)^2} \quad (8)$$

where R is the resistance of the sample, ω is the angular frequency and τ is the relaxation time (RC). τ is calculated by an expression $\tau = R_gC_g$, where R_g and C_g are the grain resistance and grain capacitance, respectively, which are arranged in parallel circuit. These parameters are obtained from Zview software and provided in Table 3.

The complex impedance measurement of the $Sr_2Ni_{1-x}Zn_xTeO_6$ (x = 0.0, 0.2, 0.4, 0.6, 0.8, 1.0) double perovskite compounds were conducted from 1 Hz to 0.1 MHz in the temperature of 298 K. Fig. 7(a) depicts the variation of real part of impedance (Z') with frequency. Z' for all samples are stable up to low frequency (~100 Hz) and reduces with the increase in frequency. The reduction of Z' values indicates an increase in AC conductivity as the frequency increases.[27,28] At nearly about 90 Hz frequency, all curves of Z' start to merge, revealing that the liberation of space charges causes the increase in AC conductivity in the compound.[29] Fig. 7(b) illustrates the variation of imaginary part of impedance (Z'') with frequency at a temperature of 298 K. A single peak present in the graph indicates the presence of one dielectric relaxation within the double-perovskite materials. The dominant relaxation involved is due to interface effect. The considerable decrease in Z'_{max} and Z''_{max} values for rich codoping Zn compositions might be due to the decrease in grain resistance (R_g). These results suggest that doping of Zn into the Sr_2NiTeO_6 remarkably affect the electrical microstructure. Suman Rani *et al.* reported that the electrical microstructure properties of doped compositions substantially change with the increase in Zn concentration in perovskite lattice.[30]

The Cole–Cole plot is presented by semicircle arcs. In this case, the plot only consists of a single semicircle arc, indicating a single phase contribution to the electrical behaviour within the sample. The fitting of the experiment data was carried out by using Zview software. The circuit used to fit the results is shown as an inset to Fig. 8. The circuit used to fit the semicircle arc consists of a single RC circuit, which represents the interface of the material.[31] The constant phase element was used in circuit instead of capacitance to accommodate nonideal capacitive behaviour due to the inhomogeneous interface. The scattered symbols in Fig. 8 indicate experimental data, whereas the solid green lines show the fitted results obtained from circuit used by Zview software. Debye stated that a perfect Debye type relaxation phenomenon shows the centre of the semicircles coincide with the real impedance axis. Thus, the Cole–Cole plot of all compounds in Fig. 8 disobey the Debye type of relaxation phenomena due to the imperfection of the sample.[32] The obtained parameters from the fitting are listed in Table 3 for all samples. The decrease of grain resistance (R_g) as Zn concentration increases has been discussed in the previous section. The values of capacitance in the range of 10^{-11} F are correlated with the interface or grain boundary, suggesting the presence of interface effects in the samples.[28]

Dielectric study

The dielectric analysis of the compound can be explained by the complex permittivity having real and imaginary parts, as shown in eqn (9)–(11):

$$\varepsilon^*(\omega) = \varepsilon'(\omega) + j\varepsilon''(\omega) \quad (9)$$

$$\varepsilon'(\omega) = \frac{Z''}{\omega\varepsilon_0 G|Z|^2} \quad (10)$$

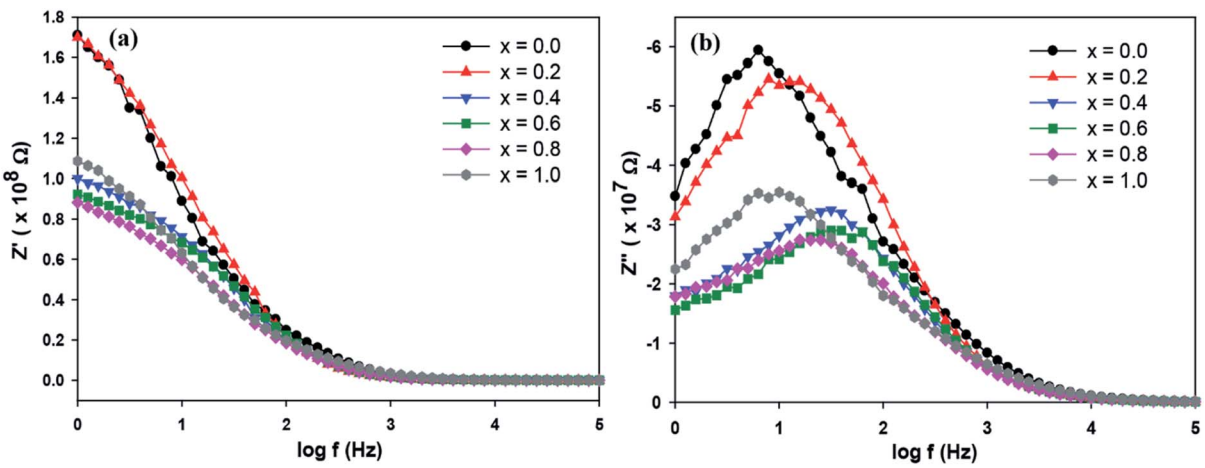

Fig. 7 (a) Variation of Z' and (b) Z'' with frequency for $SrNi_{1-x}Zn_xTeO_6$ (x = 0.0, 0.2, 0.4, 0.6, 0.8 and 1.0) at temperature 298 K.

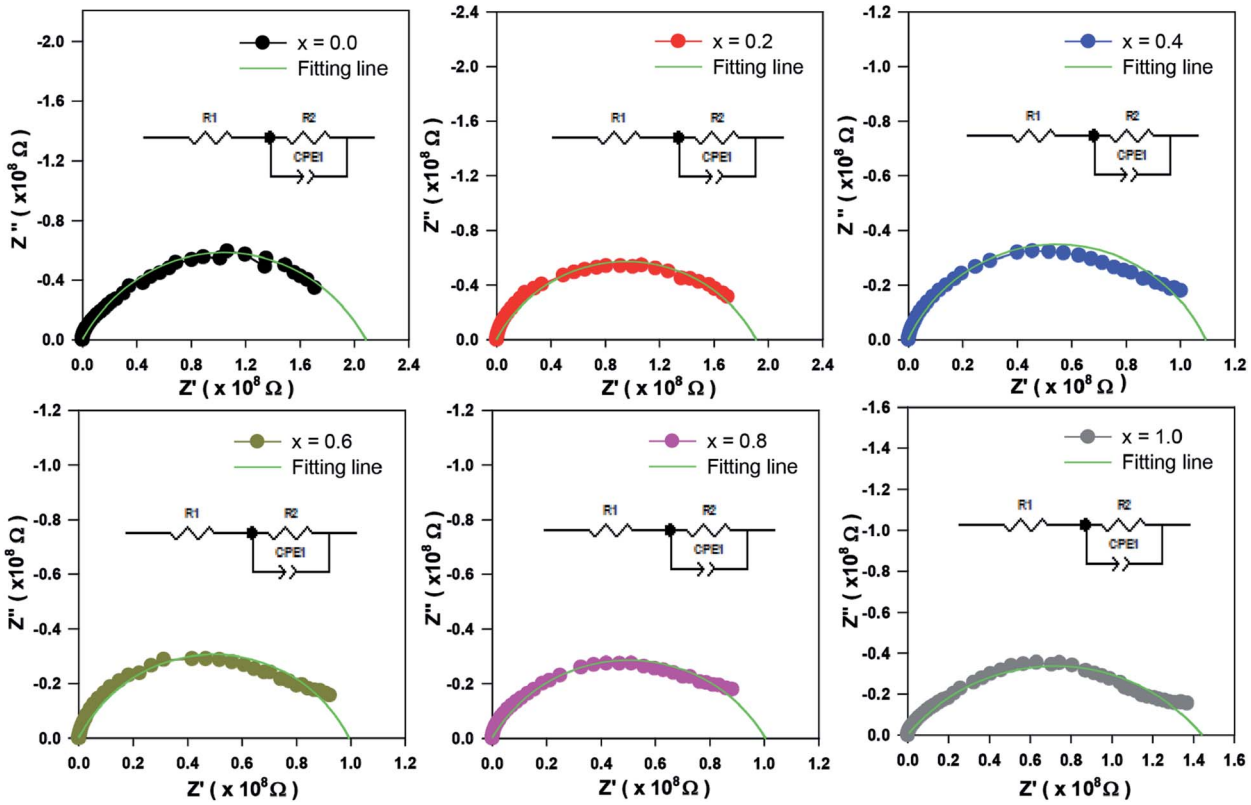

Fig. 8 Cole–Cole plots for $Sr_2Ni_{1-x}Zn_xTeO_6$ (x = 0.0, 0.2, 0.4, 0.6, 0.8 and 1.0).

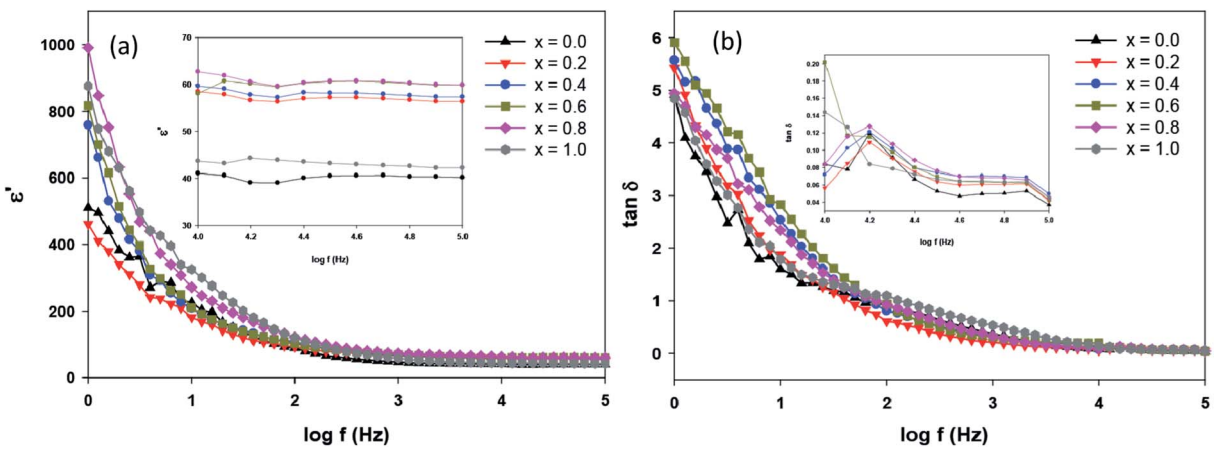

Fig. 9 (a) Frequency dependence of ε' and (b) tan δ for $Sr_2Ni_{1-x}Zn_xTeO_6$ (x = 0.0, 0.2, 0.4, 0.6, 0.8 and 1.0) at 298 K (inset represents the zoom view of frequency range from 10^4 Hz to 10^5 Hz).

$$\varepsilon'(\omega) = \frac{Z''}{\omega\varepsilon_0 G|Z|^2} \quad (11)$$

where $\varepsilon'(\omega)$ is the dielectric constant as a function of angular frequency (ω), which indicates the energy stored, and $\varepsilon''(\omega)$ is the energy loss during every cycle of electric field. Z' and Z'' are real and imaginary components of impedance, respectively. ε_0 is the absolute permittivity (8.85×10^{-12} C^2 N^{-1} m^{-1}), and G is the area of electrode per thickness of pellet sample. Dependency of ε' and ε'' with frequency are correlated with various polarisation effects – ionic, dipolar, electronic and space charge that appears at multiple levels of material reaction due to short and long-range movement of mobile charges.[33] The real component of dielectric (ε') indicates the ability of the electrical dipoles within the sample to align with the external electric field, whereas imaginary component of dielectric (ε'') indicates the energy dissipation in the compound. The frequency dependence of dielectric constant, ε', and tangent loss, tan δ, of the $Sr_2Ni_{1-x}Zn_xTeO_6$ compounds between range of 1 Hz to 0.1 MHz at room temperature are shown in Fig. 9(a) and (b), respectively. All

Table 4 Bulk density, ρ, dielectric constant ε' and dielectric loss tan δ at 0.1 MHz of $SrNi_{1-x}Zn_xTeO_6$ ($x = 0.0$, 0.2, 0.4, 0.6, 0.8 and 1.0)

x	Bulk density, ρ (g cm^{-1})	Dielectric constant, ε' at 0.1 MHz	Dielectric loss, tan δ at 0.1 MHz
0.0	5.701	40.2	0.04
0.2	5.818	56.4	0.04
0.4	5.894	57.3	0.05
0.6	5.937	59.9	0.04
0.8	6.008	59.9	0.05
1.0	5.818	42.2	0.05

samples show a trend similar to normal dielectric materials. At a low frequency (~1 Hz), the dielectric values are the highest for all samples because the dipoles within the samples align themselves along the applied electric field and contribute fully the total polarisation of dielectric. The high values of ε' unexpectedly observed only at very low frequencies may be attributed to the fact that the free charges build up at interfaces within the bulk of the sample (interfacial Maxwell–Wagner polarisation) and at the interface between the sample, and the electrode space-change polarisation[31] between these compounds reveal that $Sr_2Ni_{0.2}Zn_{0.8}TeO_6$ has the highest dielectric value (991.9 ± 0.1) and dielectric loss (5.9 ± 0.1) at 1 Hz.

These results suggest that codoping of Zn into the Sr_2NiTeO_6 may be attributed to the low grain resistance, which allows the charge carriers to respond to an electric field, as listed in Table 3.[30] In addition, the dependency of frequency and dielectric constant show milder decrease for Sr_2NiTeO_6 and $Sr_2Ni_{0.8}Zn_{0.2}TeO_6$, representing its better perspective for electronic applications.[33] At a high frequency (~100 Hz), the variation in the field is very rapid for the electrical dipoles and unable to realign themselves. Hence, dielectric permittivity can become negligible, resulting in the decrease of dielectric constant ε' with increasing frequency. The values of bulk density, dielectric constant and dielectric loss for each samples are tabulated in Table 4. At 0.1 MHz, the $Sr_2Ni_{0.4}Zn_{0.6}TeO_6$ and $Sr_2Ni_{0.2}Zn_{0.8}TeO_6$ have the greatest ε' (59.9 ± 0.1). The highest density of $Sr_2Ni_{0.2}Zn_{0.8}TeO_6$ could explain its higher dielectric value at both regions compared with other compounds.[18]

Conclusions

In this paper, the structural and dielectric properties of polycrystalline $Sr_2Ni_{1-x}Zn_xTeO_6$ ($x = 0.0$, 0.2, 0.4, 0.6, 0.8, 1.0) were synthesised using a conventional solid-state reaction method. The sample was crystallised into a $I2/m$ monoclinic space group. SEM images revealed that the grain sizes decrease as Zn content increases, and the samples are aggregated in groups. The absorption band obtained from FTIR spectra showed that all the samples confirm the molecular bands on the perovskite oxide structure. The UV-vis analysis showed that E_g increases with increase in Zn content. The IS results confirmed that the nonDebye type of relaxation phenomena occurred for all samples. The EIS characterisation revealed that $Sr_2Ni_{0.2}Zn_{0.8}TeO_6$ double-perovskite compounds have high dielectric constants (~1000 at 1 Hz and ~60 at 10^5 Hz) and exhibit low dielectric loss (tan $\delta \leq 0.20$) in the range of 10^4–10^5 Hz frequency at room temperature. This study shows that the dielectric properties of $Sr_2Ni_{1-x}Zn_xTeO_6$ can be altered by codoping method. These materials could be promising candidates for use in electronic devices because they possess dielectric behaviour.

Author contributions

F. I. H Alias carried out the lab work, heavily participated in data analysis, drafted the manuscript; Dr R. Rajmi participated in data analysis; M. F. Maulud and Dr Z. Mohamed revised the manuscript. All authors have read and agreed to the published version of the manuscript.

Conflicts of interest

There are no conflicts to declare.

Acknowledgements

The authors would like to thanks the Centre of Nanoscience and Nanotechnology, Universiti Teknologi MARA (UiTM) for UV-vis spectroscopy. This work was financially supported by the Ministry of Higher Education (MOHE) and Universiti Teknologi MARA (UiTM) through the Fundamental Research Grant Scheme (600-IRMI/FRGS 5/3 (356/2019)).

Notes and references

1 A. A. Allah, M. Elhadi and O. A. Yassien, *Adv. Mater. Res.*, 2013, **717**, 133–138.
2 A. Zaraq, B. Orayech, J. M. Igartua and A. El Bouari, *Powder Diffr.*, 2013, **6**, 1–11.
3 A. Dias, G. Subodh, M. T. Sebastian, M. M. Lage and R. L. Moreira, *Chem. Mater.*, 2008, **20**, 4347–4355.
4 A. Dias, G. Subodh, M. T. Sebastian and R. L. Moreira, *J. Raman Spectrosc.*, 2010, **41**, 702–706.
5 R. Ubic, S. Letourneau, S. Thomas, G. Subodh and M. T. Sebastian, *Chem. Mater.*, 2010, **22**, 4572–4578.
6 M. Z. M. Halizan, Z. Mohamed and A. K. Yahya, *Mater. Res. Express*, 2020, **7**, 086301.
7 F. Zhao, Z. Yue, Z. Gui and L. I. Longtu, *Jpn. J. Appl. Phys., Part 1*, 2005, **44**, 8066–8070.
8 V. L. Vilesh and G. Subodh, *Ceram. Int.*, 2018, **44**, 12036–12041.
9 M. Z. M. Halizan, A. K. Yahya, N. B. Ibrahim, N. Ibrahim and Z. Mohamed, *Digest Journal of Nanomaterials and Biostructures*, 2020, **15**, 733–741.
10 K. I. Kobayashi, T. Kimura, H. Sawada, K. Terakura and Y. Tokura, *Nature*, 1998, **395**, 677–680.
11 M. Itoh, I. Ohta and Y. Inaguma, *Mater. Sci. Eng., B*, 1996, **41**, 55–58.
12 Y. A. Alsabah, M. S. AlSalhi, A. A. Elbadawi and E. M. Mustafa, *Materials*, 2017, **10**, 1–12.

13 K. Ramesh Kumar, N. Harish Kumar, G. Markandeyulu, J. A. Chelvane, V. Neu and P. D. Babu, *J. Magn. Magn. Mater.*, 2008, **320**, 2737–2740.
14 W. Yansen, D. Kim, K. J. Parwanta, C. Liu and B. W. Lee, *Curr. Appl. Phys.*, 2015, **15**, 120–123.
15 F. I. H. Alias, M. F. Maulud and Z. Mohamed, *AIP Conf. Proc.*, 2021, **1**, 030001.
16 B. Orayech, L. Ortega-San-Martín, I. Urcelay-Olabarria, L. Lezama, T. Rojo, M. I. Arriortua and J. M. Igartua, *Dalton Trans.*, 2016, **45**, 14378–14393.
17 D. D. Han, W. Gao, N. N. Li, R. L. Tang, H. Li, Y. M. Ma, Q. L. Cui, P. W. Zhu and X. Wang, *Chin. Phys. B*, 2013, **22**, 059101.
18 M. Z. M. Halizan, Z. Mohamed and A. K. Yahya, *Sci. Rep.*, 2021, **11**, 1–13.
19 C. Lan, S. Zhao, T. Xu, J. Ma, S. Hayase and T. Ma, *J. Alloys Compd.*, 2016, **655**, 208–214.
20 G. Blasse and A. F. Corsmit, *J. Solid State Chem.*, 1973, **6**, 513–518.
21 M. Gateshki, J. M. Igartua and E. Hernández-Bocanegra, *J. Phys.: Condens. Matter*, 2003, **15**, 6199–6217.
22 M. Z. M. Halizan, Z. Mohamed and A. K. Yahya, *AIP Conf. Proc.*, 2021, **1**, 030005.
23 Y. A. Alsabah, A. A. Elbadawi, E. M. Mustafa and M. A. Siddig, *J. Mater. Sci. Chem. Eng.*, 2016, **04**, 61–70.
24 Y. A. Alsabah, M. S. AlSalhi, E. M. Mustafa, A. A. Elbadawi, S. Devanesan and M. A. Siddig, *Crystals*, 2020, **10**, 299.
25 N. A. F. M. Saadon, N. M. Ali, N. Ibrahim and Z. Mohamed, *AIP Conf. Proc.*, 2021, **1**, 030006.
26 H. W. Eng, P. W. Barnes, B. M. Auer and P. M. Woodward, *J. Solid State Chem.*, 2003, **175**, 94–109.
27 B. N. Parida, N. Panda, R. Padhee, P. R. Das and R. N. P. Choudhary, *J. Mater. Sci.: Mater. Electron.*, 2017, **28**, 1824–1831.
28 Z. Imran, M. A. Rafiq and M. M. Hasan, *AIP Adv.*, 2014, **4**, 13.
29 R. Das and R. N. P. Choudhary, *J. Mater. Sci.: Mater. Electron.*, 2018, **29**, 19099–19110.
30 S. Rani, N. Ahlawat, R. Punia, K. M. Sangwan and P. Khandelwal, *Ceram. Int.*, 2018, **44**, 23125–23136.
31 D. K. Mahato, A. Dutta and T. P. Sinha, *Bull. Mater. Sci.*, 2011, **34**, 455–462.
32 R. Das and R. N. P. Choudhary, *J. Adv. Ceram.*, 2019, **8**, 174–185.
33 J. Bijelić, D. Tatar, S. Hajra, M. Sahu, S. J. Kim, Z. Jagličić and I. Djerdj, *Molecules*, 2020, **25**, 3996.